Silicon nitride nanobeam enhanced emission from all-inorganic perovskite nanocrystals

CHEE FAI FONG,[1,7] YIN YIN,[1,7] YUEYANG CHEN,[2] DAVID ROSSER,[3] JUN XING,[1,4] ARKA MAJUMDAR,[2,3,8] AND QIHUA XIONG[1,5,6,9]

[1]*Division of Physics and Applied Physics, School of Physical and Mathematical Sciences, Nanyang Technological University, 637371, Singapore*
[2]*Electrical and Computer Engineering, University of Washington, Seattle, WA 98195, USA*
[3]*Department of Physics, University of Washington, Seattle, WA 98195, USA*
[4]*Currently with Key Laboratory of Eco−Chemical Engineering, Ministry of Education, College of Chemistry and Molecular Engineering, Qingdao University of Science and Technology, Qingdao 266042, China*
[5]*NOVITAS, Nanoelectronics Centre of Excellence, School of Electrical and Electronic Engineering, Nanyang Technological University, 639798, Singapore*
[6]*MajuLab, CNRS-UNS-NUS-NTU International Joint Research Unit, UMI 3654, 639798, Singapore*
[7]*These authors contributed equally*
[8]*arka@uw.edu*
[9]*qihua@ntu.edu.sg*

Abstract: Optically active perovskite nanocrystals have shown considerable promise for a myriad of applications, such as single photon source, light-emitting diodes and nanophotonics. Coupling those nanocrystals to photonic micro- and nanostructures will offer additional degrees of freedom to manipulate their optical properties. Herein, we demonstrate the coupling of perovskite nanocrystals to a mechanically robust, poly(methyl-methacrylate) (PMMA)-encapsulated silicon nitride nanobeam photonic crystal cavity at room temperature. As determined from the time-resolved photoluminescence decay measurements, we observed enhanced spontaneous emission from the perovskite nanocrystals by a factor of 1.4, consistent with finite difference time domain simulation. In addition, by varying the concentration of the perovskite nanocrystal in the PMMA layer, the effective index of the layer can be modified, allowing us to tune the cavity mode resonance. Our results show that solution-processable perovskite nanocrystals hold a promising prospect for applications such as on-chip light sources, optoelectronic devices and photonic integrated circuits.

1. Introduction

Halide perovskites, as a class of material, have been garnering significant attention among the research communities on their fundamental properties, as well as prospects for practical applications [1–5]. In particular, semiconductor lead halide perovskites are found to be promising for optoelectronic applications, including on-chip light sources [6–8]. The interest in lead halide perovskites partly lies in their chemical composition: YMZ_3 where Y could be an organic compound such as methylammonium or formamidinium or a cesium cation (Cs^+); M being the lead cation (Pb^{2+}); and Z is the halide anion namely chloride (Cl^-), bromide (Br^-), iodide (I^-) or a mixture, forming a typical perovskite crystalline structure. Such a chemical structure allows for wide-band emission tunability via composition stoichiometry, enabling the coverage of the whole visible spectrum. As such, lead halide perovskite could compensate for the "green gap" of conventional semiconductor such as the III-nitride and III-phosphide [4,9,10]. Colloidal perovskite nanocrystals are also superior to their traditional II-VI colloidal counterparts which tend to be difficult to synthesize and suffer from poor optical properties on the blue side of the visible spectrum [11,12].

Lead halide perovskites also exhibit several favorable properties for light emitting devices, including high photoluminescence (PL) quantum yield attributed to the low densities of defects [13,14], which reduce the nonradiative loss via carrier trapping. The large stokes shift in the emission of these perovskites also reduces the carrier loss to detrimental reabsorption [15]. Combined with the large exciton binding energy, indeed, there have been many demonstrations of perovskite light emitting devices such as LED and lasers capable of operating at room temperature [16–25].

Efforts to utilize perovskite in devices to manipulate their optical properties inevitably involve the tweaking the dimensionality of the perovskite sample [26–29], patterning of micro/nanostructures onto perovskites [30–32] or coupling the perovskites to micro/nanostructures [33–35]. For example, the coupling of perovskite nanocrystals to a nanobeam photonic crystal (PhC) cavity is promising as the localization of waves in the small mode volume cavity could enable the miniaturization of light source or photonic devices useful for integrated photonic circuits. However, the conventional air-suspended nanobeam suffers from the lack of mechanical stability which hampers a more widespread adoption.

To circumvent this problem, we design and fabricate a silicon nitride (SiN) nanobeam which sits on top of an oxide substrate [36] as opposed to the conventional air-suspended configuration. This enables us to spin-coat a layer of poly(methyl-methacrylate) (PMMA) mixed with all-inorganic $CsPbBr_3$ perovskite nanocrystals to encapsulate the nanobeam (Fig. 1) – a step which could damage the air-suspended nanobeam. We demonstrate a facile way to tune the cavity mode resonance: by varying the concentration of the perovskite nanocrystal in the PMMA layer, the effective index of the layer can be modified, allowing us to tune the cavity mode resonance. We then verify the coupling of the perovskite nanocrystals to the cavity at room temperature and observed the enhancement of the spontaneous emission from the perovskite nanocrystal by a factor of ~1.4, consistent with expectations based on numerical simulations. Our results highlight the prospects of using solution processable perovskite nanocrystal for a mechanically robust on-chip photonic device with a small footprint.
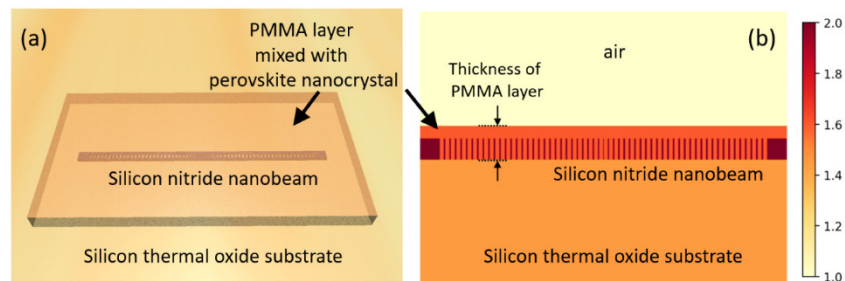
Fig. 1. Schematic of the perovskite nanocrystal coupled SiN nanobeam photonic crystal cavity. (a) 3D rendering of the SiN nanobeam on a substrate encapsulated with a PMMA layer mixed with perovskite nanocrystal as labelled. The SiN nanobeam sits on top of an oxide substrate giving it mechanical robustness. (b) A cross-sectional view along the length of the nanobeam illustrating the various materials with the colors indicating the respective material index. Here, the PMMA layer is set to have an index of 1.6 to distinguish it from the substrate with index of 1.45. The thickness of the PMMA layer in the FDTD simulation is the length from the surface of the substrate to the top of the PMMA layer. The holes of the nanobeam are taken to be filled with material of the same index as that of the PMMA layer.

2. Silicon nitride photonic crystal cavity

As described in our previous works [36,37], to design the nanobeam resonators, we first simulated the photonic band structure using the MIT Photonic Bands (MPB) software package and then optimized the characteristics of the optical cavity via finite difference time

domain (FDTD) calculations with Lumerical FDTD solutions. The calculations here were carried for a SiN (index, n = 2) nanobeam completely surrounded by a material of n = 1.45 of effectively infinite thickness above and below the nanobeam. The optimized design of the SiN nanobeam resonators consist of elliptical holes with a period, a = 157 nm, major and minor diameters being 202 nm and 100 nm respectively, with 40 such holes forming the Bragg region on each side of the nanobeam. The cavity is formed by linearly tapering both the period and the major axis of the 10 holes approaching the center from each side, as shown schematically in Fig. 2(a). The innermost elliptical holes have a minimum period and major diameter of 146 nm and 150.4 nm respectively. The minor diameter of the holes is kept constant throughout the nanobeam. The edge-to-edge gap of the two innermost holes is 78.3 nm. The nanobeam has a thickness of 220 nm and a width of 450 nm. We obtained the fundamental mode – which is the mode of interest – with resonant wavelength, λ_{cav}~520 nm at which the CsPbBr$_3$ perovskite nanocrystals tend to exhibit the most intense PL. The simulated electric field intensity distribution of the fundamental mode is shown in Fig. 2(b). The simulated cavity Q-factor is about 200,000 with a mode volume of ~3$(\lambda/n)^3$. However, to accommodate two grating couplers and their associated tapers within the field of view within the confocal microscope for the initial characterization of the cavity mode, the overall resonator size is reduced such that each Bragg region consist of 20 holes instead of 40. This results in a reduced Q-factor of ~9000 while keeping a similar resonant wavelength and mode volume.

The nanobeam PhC cavities were fabricated using a 220 nm thick SiN membrane (refractive index ~2.0) grown via LPCVD on thermal oxide of silicon. A layer of roughly 400 nm thick Zeon ZEP520A resist is deposited onto the SiN membrane with a spin-coater. The resist was also coated with a thin layer of Pt/Au which served as a charge dissipation layer. This is followed by the patterning of the resist using a JEOL JBX6300FX with an accelerating voltage of 100 kV. The pattern was then transferred to the SiN by reactive ion etching using CHF$_3$/O$_2$. More specific details of the fabrication and characterization of such nanobeam PhC cavities can be found in our previous work [36].

3. Coupling perovskite nanocrystal to encapsulated SiN nanobeam PhC cavity

The CsPbBr$_3$ Perovskite nanocrystals were dispersed in toulene and were synthesized following the procedures described in [38]. The perovskite nanocrystal solution was then mixed with PMMA formulated in anisole (MicroChem 950PMMA A4). We prepared solutions of perovskite nanocrystals with different concentrations. We injected a varying amount of anisole (Aldrich, anhydrous 99.7%) – 0 ml, 5 ml and 10 ml – to a fixed 10 ml of PMMA solution before mixing with about 0.1 ml of perovskite nanocrystal solution. With increasing volume of anisole, the solution becomes more dilute and the concentration of perovskite nanocrystals in PMMA is reduced. To couple the perovskite to the cavity, the solution was then spin-coated on the nanobeam sample at 4000 rpm for 1 minute, which effectively places the nanocrystals on the cavity and at the same time encapsulating the nanobeam. Taking the thickness of the PMMA layer to be the length from the surface of the substrate to the top of the PMMA layer, the thickness is expected to be about 400 nm in accordance to the manufacturer data sheet. Figure 2(c) shows the scanning electron micrograph (SEM) of the PMMA encapsulated nanobeam.
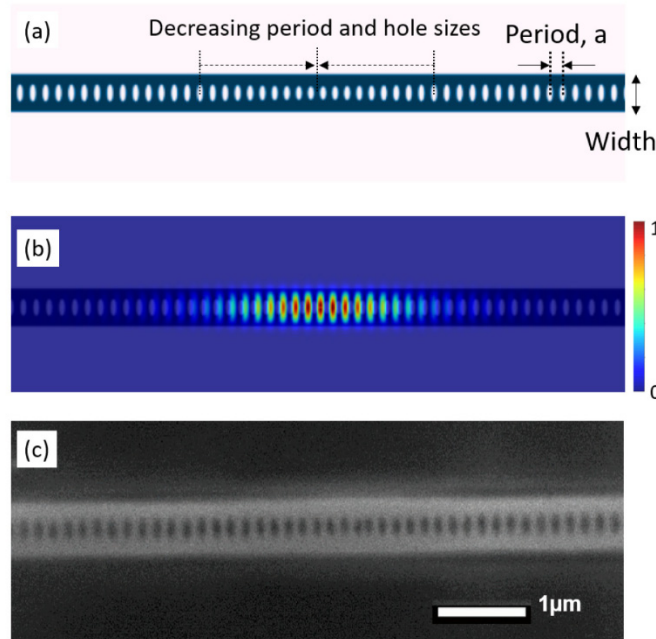
Fig. 2. Characteristics of the SiN nanobeam. (a) Schematic of the nanobeam with elliptical holes with the parameters period, a and width labelled. The cavity is formed by linearly reducing both the hole period and the major axis of the 10 holes at the center on each side of the nanobeam as indicated by the dashed arrows (see main text for the parameter values). (b) Simulated electric field intensity distribution of the fundamental cavity mode. (c) Scanning electron micrograph (SEM) of the PMMA encapsulated SiN nanobeam. As the PMMA layer is nonconductive, the resulting SEM image is less sharp. Nonetheless, the edges of the nanobeam, as well as the linearly decreasing hole sizes can be clearly seen in the image.

Optical experiments on the samples were carried out in a confocal microscopy system at room temperature. For the time-averaged measurements, a continuous wave He-Cd laser excitation at 442 nm was focused (100 × objective lens, NA = 0.90) onto the sample. The emission spectra were measured with a Horiba HR Evo spectrometer with a focal length of 800 mm together with a 300 lines/mm grating and a liquid nitrogen cooled Si CCD detector. For time-resolved decay measurements, a Ti:sapphire femtosecond-pulsed laser with ~100 fs pulses at 80 MHz was used. The emission of the laser was frequency doubled to output 400 nm pulses. The emission from the sample was detected with an avalanche photon detector (Micro Photon Devices) connected to a single photon counting module (PicoHarp 300). The overall temporal resolution of the time-resolved setup was measured to be about 22 ps.

Figure 3(a) shows a series of spectra corresponding to PMMA layers with decreasing perovskite nanocrystal concentration. The PL emission of the $CsPbBr_3$ perovskite nanocrystals is centered at 520 nm. The spectra also show the narrow cavity mode resonances at longer wavelengths relative to the perovskite nanocrystal emission as indicated by the arrows above the peaks. The background PL in the spectra can be attributed to emission from the perovskite nanocrystals which are not coupled to the cavity as well as the scattered light off the nanobeam.

To further study the coupling between the perovskite nanocrystal with the encapsulated nanobeam, we spin-coated the PMMA mixed with perovskite solution of different concentrations. As the perovskite nanocrystal in the PMMA layer decreases, we found that cavity mode resonance becomes increasingly blue-shifted. We attribute the blue-shift of the mode resonance to the change in the effective index of the encapsulating PMMA. Decreasing concentration of $CsPbBr_3$ (refractive index ~2.6) in PMMA (refractive index~1.49) will result

in the overall decrease in the effective index of the encapsulating layer of the nanobeam, and blue-shift the cavity mode. By peak fitting, we could also extract the mode wavelength, λ_{cav} and the linewidth at full-width half-maximum ($\Delta\lambda_{FWHM}$) to determine the experimental Q = $\lambda_{cav}/\Delta\lambda_{FWHM}$ of the cavity modes. The extracted Q-factors for the spectra increases from ~900 to ~1500 with decreasing perovskite concentration. The experimental Q-factors are smaller than that obtained in the simulations, which we attribute to the fabrication imperfection due to the small nanobeam feature sizes necessary for operation in the 500 nm wavelength regime.
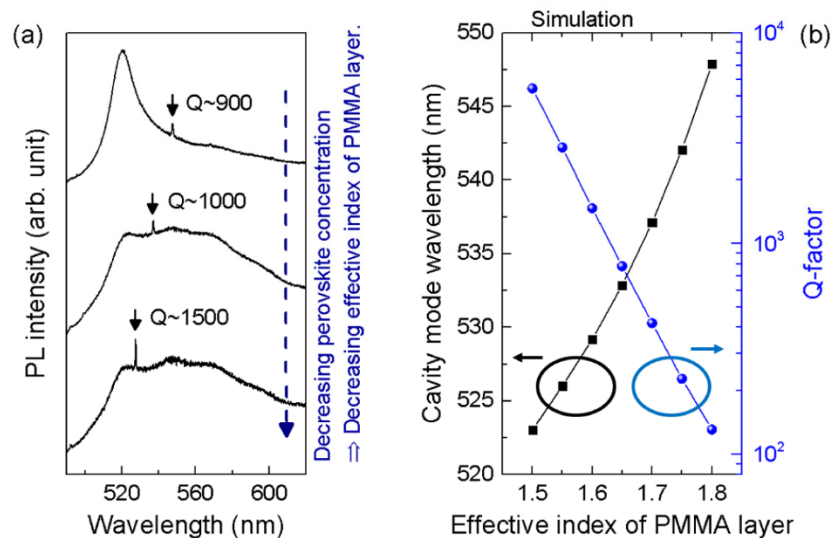
Fig. 3. Tuning of cavity mode resonance (a) A series of spectra under around 15 μW of CW laser excitation corresponding to the decreasing perovskite concentration in the direction of the dashed arrow. The spectra show the broad perovskite PL emission peak center at 520 nm and the narrow cavity mode resonances as indicated by the arrows along with the respective Q-factors. The mode resonant wavelength decreases with the decreasing concentration of perovskites in the PMMA layer. (b) The simulated cavity mode resonant wavelength (black squares) decreases with the decrease of the effective index of the PMMA layer, while the Q-factor (blue spheres) shows the opposite trend.

To explain the experimental observations, we carried out further FDTD simulations with MEEP [39] software package in which we model a nanobeam being encapsulated by a layer of PMMA with a finite thickness (Fig. 1(b)) as in the experiments. We simulated the change in the concentration of perovskite nanocrystals in the PMMA layer by varying the index value of the top PMMA layer encapsulating the nanobeam structure. The holes of the nanobeam are taken to be filled with material of the same index as that of the PMMA layer. The main simulation results are summarized in Fig. 3(b). Indeed, the simulated mode resonance wavelength exhibits a monotonic decreasing trend with the reduction of the effective index of the PMMA layer, consistent with experimental observation. Furthermore, the simulated Q-factor increases with the decrease of the effective index of the PMMA layer supporting our experimental observations. The decrease of the effective index of the PMMA layer raises the index contrast between the layer and the nanobeam, thus the higher Q-factor.

The dilution of PMMA with additional anisole (lowering the concentration of perovskite nanocrystal) could also reduce the thickness of the PMMA layer. To rule out the possibility that the change in the cavity mode resonant wavelength is due to the change in the PMMA thickness, we performed simulations for PMMA layer thicknesses of 250 nm, 400 nm and 600 nm. Figure 4 summarizes the cavity mode wavelength and the Q-factor of the simulation results. Overall, for all values of the effective index, the cavity mode wavelength increases with a thicker PMMA layer. The increase in the mode wavelength with thickness is more

significant at larger effective index. Given the values of the Q-factors, the shift of the mode wavelength with changing thickness should be larger or comparable to its linewidth and thus would be observable spectrally. Nonetheless, the variation in the mode wavelength due to PMMA thickness is well within 10 nm for most values of the effective index of the PMMA layer such that it could not account for the large shift observed in the experiments. Therefore, we attribute the experimentally observed shift in the mode wavelength mainly to the varying effective index of the encapsulating PMMA layer.

Instead of changing the effective index of the PMMA layer by diluting the PMMA solution, one could also dilute the perovskite nanocrystal solution while keeping a fixed PMMA concentration. With the same spin coating conditions, one would get consistent PMMA layer thicknesses regardless of its effective index and could thus eliminate the effect of layer thickness on the cavity mode wavelength.
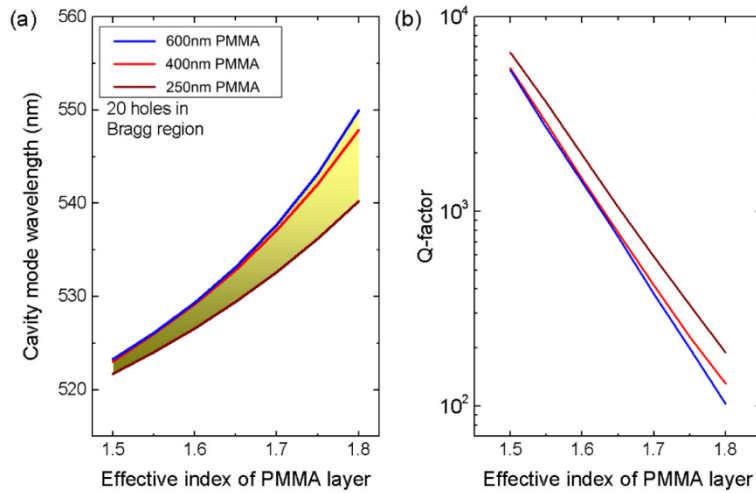
Fig. 4. (a) The plot shows the change in the cavity mode wavelength with the effective index of the PMMA layer for different PMMA layer thicknesses, namely 250 nm, 400nm and 600nm. Depending on the actual thickness of the PMMA layers prepared experimentally, the cavity mode wavelength could take a value within the region marked in yellow. (b) As for the Q-factor, the thicker PMMA layers cause a drop in the Q-factors, with a larger effect at higher effective index.

It is worth highlighting that measurements were performed on the same nanobeam resonator. Aside from the changing Q-factor because of the varying effective index of the PMMA layer, the cavity showed no significant degradation despite having undergone multiple rounds of sonication with acetone and spin coating of the PMMA layer, proving that the nanobeam PhC cavity is structurally robust. This tuning method of the mode resonance via the effective index around the cavity environment could be useful for the coupling of other colloidal quantum emitters to cavities, possibly with other types of capping layer beside PMMA.

To verify the spontaneous emission enhancement of the perovskite nanocrystal coupled with the cavity, we measured the time-resolved PL decay of the perovskite emission. The PL decay curves of the perovskite emission from the coupled and uncoupled cases are presented in Fig. 5. The perovskite nanocrystal PL exhibits a multiexponential decay due to a distribution of the nanocrystal parameters such as size and nonradiative decay rate [40]. Assuming that the perovskite nanocrystals ensemble consists of 3 main subpopulations, each with a characteristic decay behavior, the decay curves were most accurately fitted with a three exponential decay function: $I(t) = I_0 + A_1 e^{-[(t-t_0)/t_1]} + A_2 e^{-[(t-t_0)/t_2]} + A_3 e^{-[(t-t_0)/t_3]}$ where $I(t)$ is the PL intensity at time t, I_0 is the background intensity, t_0 is the temporal offset relative to 0

when the decay begins and t_i (A_i) with i = 1, 2, 3 being the three decay time constant (amplitude). We take the shortest decay time t_1 as the representation radiative lifetime since the fractions of the amplitude, $A_1/(A_1 + A_2 + A_3)$ is close to 1 in both the coupled and uncoupled cases, implying that the subpopulation of the nanocrystal with characteristic decay time t_1 is dominant. The t_1 times are extracted to be 0.65 ± 0.04 ns and 0.46 ± 0.03 ns respectively for the coupled and uncoupled cases, consistent with previous report [41]. Taking the ratio of t_1 of the uncoupled case to that of the coupled case, we obtained a Purcell factor of 1.4 ± 0.8, indicating the enhancement of spontaneous emission.
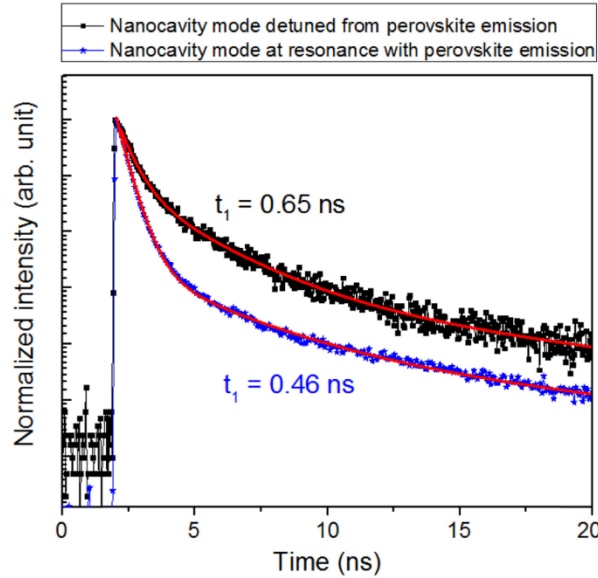
Fig. 5. Plot comparing the PL decay of the perovskite nanocrystals in two different cases: one which is coupled to the cavity (blue) and the other uncoupled (black) with the respective t_1 decay time as labelled.

To estimate the theoretical Purcell enhancement based on the FDTD simulations, we employ the following equation for the Purcell factor [42]: $F_p = 1 + \frac{3\lambda_{cav}^3}{4\pi^2 n^2} \frac{Q_e}{V_{mode}} |E|_{local}^2$ where λ_{cav} is the mode resonant wavelength, n is the refractive index of SiN, Q_e is the Q-factor of the emitter and V_{mode} being the mode volume. In consideration of the local density of states, one would also need to factor in the local electric field intensity expressed as $|E|_{local}^2 = |E(\mathrm{r})|^2 / |E(\mathrm{r})|_{max}^2$ where r is the position of the emitter. We note that this model of Purcell factor is appropriate for our experiments since the emitter emission linewidth is larger than that of the cavity mode linewidth. In this case, the Purcell factor depends on the Q-factor of the emitter and not that of the cavity. By performing multiple peak fit to the spectra of the uncoupled case, the full-width at half-maximum linewidth of the perovskite nanocrystal emission was found to be 20 nm and thus giving a Q-factor of about 26. From the FDTD simulations, V_{mode} was found to be ~$3(\lambda/n)^3$. Assuming that the emitter is located at the center of the nanobeam cavity on the surface gives $|E|_{local}^2 = 0.26$. The resulting Purcell factor is obtained to be 1.34 consistent with experimental results.

4. Conclusions

We have demonstrated the coupling of perovskite nanocrystal to a PMMA encapsulated SiN nanobeam PhC cavity at room temperature, enhancing the spontaneous emission from the perovskite by a factor of 1.4. The Purcell factor could be further increased by improving the

design of the cavity to obtain lower mode volumes and/or enhancing the electric field at the surface where the emitters are coupled. In addition, we showed the effective tuning of the cavity mode resonance by changing the effective index of the encapsulating PMMA layer via varying the concentration of perovskite nanocrystal. This method of tuning could be useful for other types of colloidal quantum emitters and cavities. Combined with the mechanically robust encapsulated nanobeam, our results show that solution processable perovskite nanocrystals could prove to be a viable alternative to the commonly used epitaxially grown light emitting materials for applications such as on-chip light source, optoelectronic devices and photonic integrated circuits. Furthermore, the coupling of perovskite nanocrystal to an encapsulated nanobeam cavity could be a promising platform to study solid-state quantum electrodynamics in the strong light-matter interaction regime.

Funding

Acknowledgments

References

1. T. Thu Ha Do, A. Granados del Águila, C. Cui, J. Xing, Z. Ning, and Q. Xiong, "Optical study on intrinsic exciton states in high-quality $CH_3NH_3PbBr_3$ single crystals," Phys. Rev. B **96**(7), 075308 (2017).
2. C. Yin, L. Chen, N. Song, Y. Lv, F. Hu, C. Sun, W. W. Yu, C. Zhang, X. Wang, Y. Zhang, and M. Xiao, "Bright-exciton fine-structure splittings in single perovskite nanocrystals," Phys. Rev. Lett. **119**(2), 026401 (2017).
3. S.-T. Ha, R. Su, J. Xing, Q. Zhang, and Q. Xiong, "Metal halide perovskite nanomaterials: synthesis and applications," Chem. Sci. (Camb.) **8**(4), 2522–2536 (2017).
4. K. Lin, J. Xing, L. N. Quan, F. P. G. de Arquer, X. Gong, J. Lu, L. Xie, W. Zhao, D. Zhang, C. Yan, W. Li, X. Liu, Y. Lu, J. Kirman, E. H. Sargent, Q. Xiong, and Z. Wei, "Perovskite light-emitting diodes with external quantum efficiency exceeding 20 per cent," Nature **562**(7726), 245–248 (2018).
5. Y. Fu, H. Zhu, J. Chen, M. P. Hautzinger, X.-Y. Zhu, and S. Jin, "Metal halide perovskite nanostructures for optoelectronic applications and the study of physical properties," Nat. Rev. Mater. **4**(3), 169–188 (2019).
6. M. A. Green, A. Ho-Baillie, and H. J. Snaith, "The emergence of perovskite solar cells," Nat. Photonics **8**(7), 506–514 (2014).
7. B. R. Sutherland and E. H. Sargent, "Perovskite photonic sources," Nat. Photonics **10**(5), 295–302 (2016).
8. Q. Zhang, R. Su, W. Du, X. Liu, L. Zhao, S. T. Ha, and Q. Xiong, "Advances in Small Perovskite-Based Lasers," Small Methods **1**(9), 1700163 (2017).
9. E. Taylor, P. R. Edwards, and R. W. Martin, "Colorimetry and efficiency of white LEDs: Spectral width dependence," Phys. Status Solidi., A Appl. Mater. Sci. **209**(3), 461–464 (2012).
10. M. Auf der Maur, A. Pecchia, G. Penazzi, W. Rodrigues, and A. Di Carlo, "Efficiency drop in green InGaN/GaN light emitting diodes: the role of random alloy fluctuations," Phys. Rev. Lett. **116**(2), 027401 (2016).
11. V. I. Klimov, "Spectral and dynamical properties of multiexcitons in semiconductor nanocrystals," Annu. Rev. Phys. Chem. **58**(1), 635–673 (2007).
12. K. Susumu, L. D. Field, E. Oh, M. Hunt, J. B. Delehanty, V. Palomo, P. E. Dawson, A. L. Huston, and I. L. Medintz, "Purple-, blue-, and green-emitting multishell alloyed quantum dots: synthesis, characterization, and application for ratiometric extracellular pH sensing," Chem. Mater. **29**(17), 7330–7344 (2017).
13. R. E. Brandt, V. Stevanović, D. S. Ginley, and T. Buonassisi, "Identifying defect-tolerant semiconductors with high minority-carrier lifetimes: beyond hybrid lead halide perovskites," MRS Commun. **5**(2), 265–275 (2015).
14. G. Xing, N. Mathews, S. S. Lim, N. Yantara, X. Liu, D. Sabba, M. Grätzel, S. Mhaisalkar, and T. C. Sum, "Low-temperature solution-processed wavelength-tunable perovskites for lasing," Nat. Mater. **13**(5), 476–480 (2014).
15. J. Q. Grim, S. Christodoulou, F. Di Stasio, R. Krahne, R. Cingolani, L. Manna, and I. Moreels, "Continuous-wave biexciton lasing at room temperature using solution-processed quantum wells," Nat. Nanotechnol. **9**(11), 891–895 (2014).
16. Y. Wang, X. Li, J. Song, L. Xiao, H. Zeng, and H. Sun, "All-inorganic colloidal perovskite quantum dots: a new class of lasing materials with favorable characteristics," Adv. Mater. **27**(44), 7101–7108 (2015).

17. S. Yakunin, L. Protesescu, F. Krieg, M. I. Bodnarchuk, G. Nedelcu, M. Humer, G. De Luca, M. Fiebig, W. Heiss, and M. V. Kovalenko, "Low-threshold amplified spontaneous emission and lasing from colloidal nanocrystals of caesium lead halide perovskites," Nat. Commun. **6**(1), 8056 (2015).
18. J. Xing, X. F. Liu, Q. Zhang, S. T. Ha, Y. W. Yuan, C. Shen, T. C. Sum, and Q. Xiong, "Vapor phase synthesis of organometal halide perovskite nanowires for tunable room-temperature nanolasers," Nano Lett. **15**(7), 4571–4577 (2015).
19. Q. Zhang, R. Su, X. Liu, J. Xing, T. C. Sum, and Q. Xiong, "High-quality whispering-gallery-mode lasing from cesium lead halide perovskite nanoplatelets," Adv. Funct. Mater. **26**(34), 6238–6245 (2016).
20. Z. Wei, A. Perumal, R. Su, S. Sushant, J. Xing, Q. Zhang, S. T. Tan, H. V. Demir, and Q. Xiong, "Solution-processed highly bright and durable cesium lead halide perovskite light-emitting diodes," Nanoscale **8**(42), 18021–18026 (2016).
21. Y. Fu, H. Zhu, C. C. Stoumpos, Q. Ding, J. Wang, M. G. Kanatzidis, X. Zhu, and S. Jin, "Broad wavelength tunable robust lasing from single-crystal nanowires of cesium lead halide perovskites (CsPbX $_3$, X = Cl, Br, I)," ACS Nano **10**(8), 7963–7972 (2016).
22. S. W. Eaton, M. Lai, N. A. Gibson, A. B. Wong, L. Dou, J. Ma, L.-W. Wang, S. R. Leone, and P. Yang, "Lasing in robust cesium lead halide perovskite nanowires," Proc. Natl. Acad. Sci. U.S.A. **113**(8), 1993–1998 (2016).
23. R. Su, C. Diederichs, J. Wang, T. C. H. Liew, J. Zhao, S. Liu, W. Xu, Z. Chen, and Q. Xiong, "Room-temperature polariton lasing in all-inorganic perovskite nanoplatelets," Nano Lett. **17**(6), 3982–3988 (2017).
24. K. Wang, S. Wang, S. Xiao, and Q. Song, "Recent advances in perovskite micro- and nanolasers," Adv. Opt. Mater. **6**(18), 1800278 (2018).
25. F. Yan, J. Xing, G. Xing, L. Quan, S. T. Tan, J. Zhao, R. Su, L. Zhang, S. Chen, Y. Zhao, A. Huan, E. H. Sargent, Q. Xiong, and H. V. Demir, "Highly Efficient Visible Colloidal Lead-Halide Perovskite Nanocrystal Light-Emitting Diodes," Nano Lett. **18**(5), 3157–3164 (2018).
26. Q. Zhang, S. T. Ha, X. Liu, T. C. Sum, and Q. Xiong, "Room-Temperature Near-Infrared High-Q Perovskite Whispering-Gallery Planar Nanolasers," Nano Lett. **14**(10), 5995–6001 (2014).
27. H. Zhu, Y. Fu, F. Meng, X. Wu, Z. Gong, Q. Ding, M. V. Gustafsson, M. T. Trinh, S. Jin, and X.-Y. Zhu, "Lead halide perovskite nanowire lasers with low lasing thresholds and high quality factors," Nat. Mater. **14**(6), 636–642 (2015).
28. B. Cai, X. Li, Y. Gu, M. Harb, J. Li, M. Xie, F. Cao, J. Song, S. Zhang, L. Cavallo, and H. Zeng, "Quantum confinement effect of two-dimensional all-inorganic halide perovskites," Sci. China Mater. **60**(9), 811–818 (2017).
29. S. Ma, M. Cai, T. Cheng, X. Ding, X. Shi, A. Alsaedi, T. Hayat, Y. Ding, Z. Tan, and S. Dai, "Two-dimensional organic-inorganic hybrid perovskite: from material properties to device applications," Sci. China Mater. **61**(10), 1257–1277 (2018).
30. K. Chen and H. Tüysüz, "Morphology-controlled synthesis of organometal halide perovskite inverse opals," Angew. Chem. Int. Ed. Engl. **54**(46), 13806–13810 (2015).
31. S. Schünemann, S. Brittman, K. Chen, E. C. Garnett, and H. Tüysüz, "Halide perovskite 3D photonic crystals for distributed feedback lasers," ACS Photonics **4**(10), 2522–2528 (2017).
32. J. Wu, J. Chen, Y. Zhang, Z. Xu, L. Zhao, T. Liu, D. Luo, W. Yang, K. Chen, Q. Hu, F. Ye, P. Wu, R. Zhu, and Q. Gong, "Pinhole-free hybrid perovskite film with arbitrarily-shaped micro-patterns for functional optoelectronic devices," Nano Lett. **17**(6), 3563–3569 (2017).
33. S. Chen, K. Roh, J. Lee, W. K. Chong, Y. Lu, N. Mathews, T. C. Sum, and A. Nurmikko, "A photonic crystal laser from solution based organo-lead iodide perovskite thin films," ACS Nano **10**(4), 3959–3967 (2016).
34. Y. Xu, Q. Chen, C. Zhang, R. Wang, H. Wu, X. Zhang, G. Xing, W. W. Yu, X. Wang, Y. Zhang, and M. Xiao, "Two-photon-pumped perovskite semiconductor nanocrystal lasers," J. Am. Chem. Soc. **138**(11), 3761–3768 (2016).
35. Z. Yang, M. Pelton, M. I. Bodnarchuk, M. V. Kovalenko, and E. Waks, "Spontaneous emission enhancement of colloidal perovskite nanocrystals by a photonic crystal cavity," Appl. Phys. Lett. **111**(22), 221104 (2017).
36. T. K. Fryett, Y. Chen, J. Whitehead, Z. M. Peycke, X. Xu, and A. Majumdar, "Encapsulated silicon nitride nanobeam cavity for hybrid nanophotonics," ACS Photonics **5**(6), 2176–2181 (2018).
37. Y. Chen, A. Ryou, M. R. Friedfeld, T. Fryett, J. Whitehead, B. M. Cossairt, and A. Majumdar, "Deterministic positioning of colloidal quantum dots on silicon nitride nanobeam cavities," Nano Lett. **18**(10), 6404–6410 (2018).
38. L. Protesescu, S. Yakunin, M. I. Bodnarchuk, F. Krieg, R. Caputo, C. H. Hendon, R. X. Yang, A. Walsh, and M. V. Kovalenko, "Nanocrystals of cesium lead halide perovskites (CsPbX$_3$, X = Cl, Br, and I): novel optoelectronic materials showing bright emission with wide color gamut," Nano Lett. **15**(6), 3692–3696 (2015).
39. A. F. Oskooi, D. Roundy, M. Ibanescu, P. Bermel, J. D. Joannopoulos, and S. G. Johnson, "Meep: A flexible free-software package for electromagnetic simulations by the FDTD method," Comput. Phys. Commun. **181**(3), 687–702 (2010).
40. N. S. Makarov, S. Guo, O. Isaienko, W. Liu, I. Robel, and V. I. Klimov, "Spectral and dynamical properties of single excitons, biexcitons, and trions in cesium–lead-halide perovskite quantum dots," Nano Lett. **16**(4), 2349–2362 (2016).
41. M. A. Becker, R. Vaxenburg, G. Nedelcu, P. C. Sercel, A. Shabaev, M. J. Mehl, J. G. Michopoulos, S. G. Lambrakos, N. Bernstein, J. L. Lyons, T. Stöferle, R. F. Mahrt, M. V. Kovalenko, D. J. Norris, G. Rainò, and A. L. Efros, "Bright triplet excitons in caesium lead halide perovskites," Nature **553**(7687), 189–193 (2018).

42. M. P. van Exter, G. Nienhuis, and J. P. Woerdman, "Two simple expressions for the spontaneous emission factor B," Phys. Rev. B Condens. Matter **54**, 6 (1996).